Simulation of finishing operations based on an implicit representation of surfaces

Charly Euzenat, Sylvain Lavernhe, Christophe Tournier

Simulation of finishing operations based on an implicit representation of surfaces

Charly Euzenat[a], Sylvain Lavernhe[a], Christophe Tournier[a]

[a] *Université Paris-Saclay, ENS Paris-Saclay, LURPA, 91190 Gif-sur-Yvette, France.*

Abstract

The manufactured surface textures after machining operations may require the use of an abrasion operation in order to meet expected requirements. In this context, the simulation of the entire manufacturing process from machining to abrasion finishing could significantly improve the parameters involved in manufacturing. The simulation of the abrasion requires to handle a high number of interactions between the workpiece and abrasive grains as well as complex mechanical behavior during material removal. Considering numerical and physical constraints, a novel model for abrasion simulations based on an implicit surface representation has been developed which allows macroscopic simulations of surface topography resulting from abrasion. The surface is embedded in a scalar field, so that the removal action occurs throughout the modification of the volumetric data rather than an explicit interaction with the surface. In this article, the implicit model is enriched in order to be able to integrate the surface topography of the previous machining operation. Thus, the simulation of the resulting surface topography for an entire manufacturing process has been performed successfully. Several experiments have been carried out and analyzed in order to evaluate the proposed model. The comparison between simulations and experimental results validates the consistency of the model regarding real abrasion finishing processes.

Keywords: abrasion simulation, finishing process, surface topography, implicit modeling

1. Introduction

The surface integrity and in particular the surface roughness is an important factor for the performances in service of mechanical parts [1]. The functional surface of parts must comply with expected requirements whether in mold and dies industry, for medical applications or for aerodynamic functions. Grinding operations are commonly used to improve the surface finish and appearance after machining [2]. In manufacturing industry, the design of the process involves several parameters in the successive operations from machining to abrasive finishing in order to achieve expected surface roughness. Contrary to machining, which mainly induces cutting, the finishing process of manufactured parts with abrasion also includes ploughing and repelling matter. These mechanisms have been described by [3] and can be classified into four main schemes. The variety in the type of defects associated with the early tool wear challenge the automation and monitoring [4] of the process. For this reason, these operations are still done manually. In this context, the prediction of geometry is often limited. An effective and relevant simulation framework for abrasion would improve production quality.

In industry, CAM software is mainly used to check the manufacturing program before machining in order to avoid unwanted collisions. The order of magnitude for surface simulation is not compatible with local marks visualization because the volume discretization is tuned to simulate a complete machining operation within minutes. The visualization of micrometric marks induced by the realistic tool geometry is possible in laboratory demonstration code [5]. The cutting action is modeled as a Boolean operation, which allows moderate simulation times and relevant surface topographies. The implemented algorithms for calculating the machined surface are based on a discretization in voxels [6], Z-buffer [7] or dexels [8] to digitally perform the intersections between the tool and the part. The performance of these methods has been demonstrated using parallel implementation on graphics processors [9]. However, the simple boolean intersection assumption is not directly applicable for abrasion simulation because of the different types of defect previously listed.

In the literature, ploughing and repelling have been taken into account with analytical models [10] or with complete material behavior modeling. Continuum mechanics simulations allow obtaining relevant output effort and surface topography as well as insight of material integrity below the surface [11, 12]. These results have been obtained for single grain indentation or scratching. Nevertheless, the computing resources required for a single grain interaction are so high that it is not possible yet to simulate a complete abrasion operation with mechanical methods. A significant number of articles assume the topography in grinding as the cinematic mapping of the grinding wheel on the surface [13, 14, 15].

A new method based on an implicit representation of surfaces [16] is developed in order to deal with more complex interactions encountered during abrasion. The simulations have been performed for the elementary polishing of a perfect plane. Results have been found promising for abrasive topography generation, however industrial applications are still limited due to the impossibility to simulate a complete manufacturing process from machining to finishing. In this article, a novel model has

been developed in order to take into account scallops generated by the milling strategy. The model is focused on simulating the overall process at a macroscopic scale.

The article is structured as follows, in section 2 a review of the literature regarding abrasion modeling and simulation techniques is presented and the core of the implicit model is presented. The contributions made to the model are presented in the section 4. Section 5 is focused on the simulation of grain paths. Finally different test cases and results are presented and discussed in 6.

2. State of the art

Abrasion is the process of wearing the surfaces in contact. In the manufacturing industry, the abrasion process is mastered and occurs with the actions of sharp particles which induce the removal of matter. These actions remain arbitrary in most cases. Models of the interactions from a local to a global order of magnitude have been developed [17]. An analysis of the defect mechanisms during polishing has been proposed by [3].

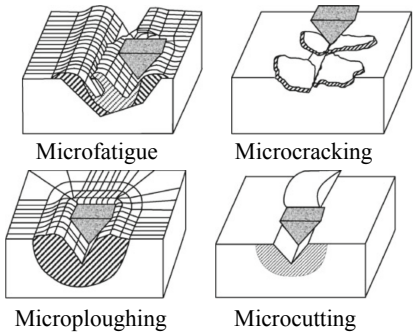

Figure 1: Abrasion defect mechanisms [3, 18]

The four types of possible interactions are pictured in (Fig. 1). Microploughing is the result of the repelling of the material on either side of the groove created by the abrasive grain. Microploughing only generates plastic deformations in the specimen, so there is theoretically no material removed. Microfatigue occurs if other grains reach the same area resulting in material failure. The microcutting is obtained in the same way as for milling by forming a chip and cutting the material. Finally, microcracking results from the stresses that are introduced into the material after repeated passage of particles. This phenomenon is observed on fragile materials while microcutting and microploughing occur during the abrasion of ductile materials. These four types of abrasion scheme happen depending on the geometry of the grain and the parameters of the interactions such as speed, penetration and contact pressure.

From an empirical point of view, several models exist. They allow predicting the evolution of the surface height as a function of time according to experimental process observations. One of the most common ones to determine the removal rate is the Preston model [19] (Eq. 1).

$$\frac{dz}{dt} = K_p.P.V \tag{1}$$

In (Eq. 1), the contact pressure P and the relative velocity V are taken into account in order to compute the wear rate of the specimen during the process. The Preston coefficient K_p is experimentally determined in order to model the efficiency of the process against its parameters. This model has been derived into more elaborate laws in order to improve the prediction relevance.

$$\frac{dz}{dt} = K_p.P^{\alpha}.V^{\beta} \tag{2}$$

Klocke [3] has developed a general-purpose model for abrasion with two additional degrees of freedom in the equation (Eq. 2). This model offers a wider range of possibilities while modeling various tool-workpiece sets. Whatever are the forms of the equations, the laws identified above are mainly used as a description of the interactions but are not yet implemented in simulations on their own.

Apart from the process driven approach, wear rate estimation can also be made from consideration of the local behavior of the grain interactions. When both cutting and repelling are combined, the profile of the groove is similar to the one presented on (Fig. 2). The fraction of cutting area f_{ab} geometrically defined by (Eq. 3) and is related to material parameters by (Eq. 4). ϕ_s is the effective deformation whereas ϕ_{lim} is the maximum deformation reachable by the material before microfatigue. The integration of the cutting area factor along the path of a particle is possible to obtain the wear rate during the process.

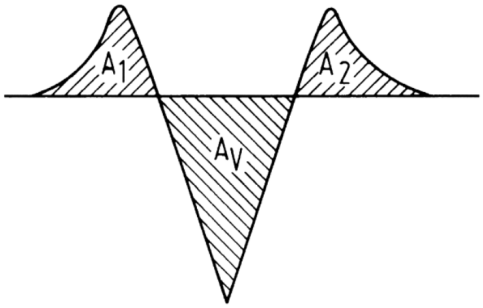

Figure 2: Drawing of the groove section with repelled matter [20]

$$f_{ab} = \frac{A_v - (A_1 + A_2)}{A_v} \tag{3}$$

$$f_{ab} = 1 - \left(\frac{\phi_{lim}}{\phi_s}\right)^{2/\beta} \tag{4}$$

Study of indentation and scratching using a complete mechanical model of the specimen has been done in the literature

[12, 11]. The resolution of the set of equations requires the use of numerical methods either based on a mesh or particles. These numerical implementations are known respectively as *finite element method* or *smooth particle hydrodynamics*. While providing valuable information concerning the strain and stress in the specimen, these algorithms imply high computational expenses, thus long simulation time. In this context, using mechanically based algorithms to simulate a complete abrasion process operation is out of reach given reasonable computing resources. Contrary to simulations based on mechanical methods which take into account microscopic interactions between the grains and the workpiece, the proposed model allows simulating surface topography at macroscopic scale.

3. Implicit abrasion approach

As stated in the literature review, boolean operations for abrasion simulation may not be sufficient in modeling all the phenomena encountered during abrasion. The microploughing which tends to repel matter aside the groove induced by the path of sharp particles requires additional modeling capabilities in the candidate model. The main idea behind the implicit model for abrasion simulation is to induce deformations of the surface by modifying the associated distance field instead of explicitly moving points on the surface. In the literature, implicit formulations have been used mainly in computer graphics to obtain deformations of objects or intuitively model surfaces [21]. Implicit surfaces can be combined with classic CSG operations or with smooth composition operators that allow complex shapes to be obtained from simple primitives [22]. The explicit simulation of material coordinates for abrasion can be made by using mechanical methods but is not possible for the complete process simulation. Thus the proposed implicit model [16] can be interposed between Boolean methods and methods based on continuum mechanics. The fundamental principles of the method are given below.

An implicit surface Γ is defined as the zeros of a scalar field function F_t. The set of points $\mathbf{X}$ which verify this equation belongs to the surface (Eq. 5) [23].

$$\Gamma(t) = \{\, \mathbf{X} \mid F_t(\mathbf{X}) \;=\; 0 \,\} \tag{5}$$

In the abrasion process, the free surface of the mechanical part evolves under the action of abrasive particles. This evolution has been modeled by means of the deformation of the scalar field F_t rather than explicitly interacting with the surface. This implicit model takes into account the fact that the abrasion topography is the result of an equilibrium between particle removal actions and the specimen strength. Considering that a scalar penalty field W_i is attached to each abrasive particle, the removal action consists in subtracting this field to the specimen. (Eq. 6) defines this temporal evolution scheme where F_t is the image of the surface according to time. In this context, a basic integration leads to (Eq. 7) which defines the evolution of F_t from initial to final time. This principle is illustrated in (Fig. 3).

It has been chosen to use a positive sign of the field inside the specimen and a negative sign on the outside.

$$F_t(\mathbf{X}) = F_{t-1}(\mathbf{X}) - W_i(\mathbf{X}) \tag{6}$$

$$F_t(\mathbf{X}) = F_{t_0}(\mathbf{X}) - \sum_i W_i(\mathbf{X}) \tag{7}$$

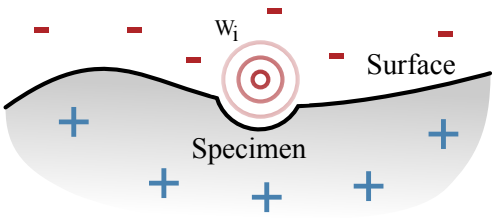

Figure 3: Principle of abrasive simulation based on implicit surfaces [16]

This scheme of surface deformation is not causal and can be implemented efficiently on parallel computational architectures. The initial scalar field F_{t_0} is responsible for the specimen behavior while the set $\{W_i \mid i \in [1;n]\}$ accounts for each abrasive particle effect on the surface.

The scalar potential W_i associated with each particle allows modeling the abrasive action on the specimen. The penalty field W_i is the composition of two functions $K \circ D$ (Eq. 8).

$$\begin{cases} K : \left| \begin{array}{ccc} \mathbb{R} & \longrightarrow & \mathbb{R} \\ l & \longmapsto & K(l) \end{array} \right. \\ D : \left| \begin{array}{ccc} \mathbb{R}^3 & \longrightarrow & \mathbb{R} \\ \mathbf{X} & \longmapsto & D(\mathbf{X}) \end{array} \right. \\ W_i : \left| \begin{array}{ccc} \mathbb{R}^3 & \longrightarrow & \mathbb{R} \\ \mathbf{X} & \longmapsto & K(D(\mathbf{X})) \end{array} \right. \end{cases} \tag{8}$$

Function K is the kernel of the abrasive grain and defines its removal influence against distance to its center l. A definition of the kernel has been proposed in [16] and follows the general rules below:

1. The action is limited within a defined range which means its potential must be zero far from its center.
2. The maximum influence is encountered close to the center of the particle.
3. Each particle has a characteristic influence radius defined by its own size.
4. The influence on the machined surface decreases with the distance.

A generic form for the particle kernel function is given in (Eq. 9) and (Fig. 4) presents these four characteristic points which lead to the general shape of an abrasive kernel given the constraints of abrasion. Three parameters $(\alpha_k, \mu_k, \sigma_k)$ are used

to define K. The intensity of the potential is given by coefficient α_k. σ_k represents the abrasive particle radius and the position of the kernel is modified with the definition of a non-zero value for μ_k.

Given the sign convention for the specimen field, the positive part of the kernel function, close to its center, removes matter from the specimen. The negative part of the curve, between point 1 and 3, allows to repel matter on the sides of the abrasive grain in order to emulate the microploughing action. Further details and elementary examples can be found in [16].

$$K(l) = \begin{cases} \sum_{k=1}^{2} \alpha_k \exp\left(-\frac{(l-\mu_k)^2}{\sigma_k^2}\right) & l \leq h \\ 0 & l > h \end{cases} \quad (9)$$

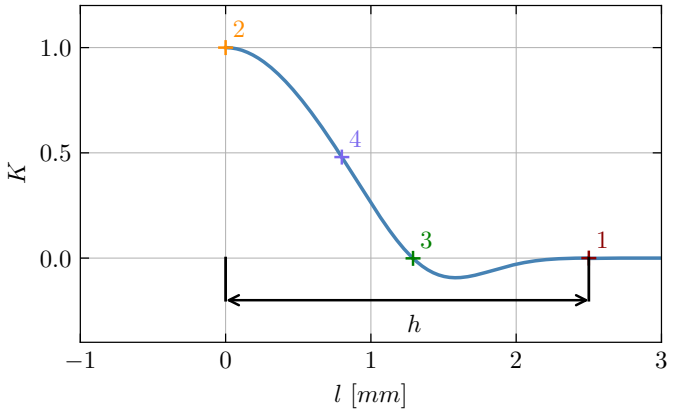

Figure 4: Gaussian kernel definition

The function D gives the distance between the particle center point $\mathbf{P}_i$ and the considered point in 3D space $\mathbf{X}$. The most simple geometrical shape for each grain is the sphere. Thus, the passage of a grain is simulated in a single operation by using the distance to a line passing by point $\mathbf{P}_i$ and directed by its unit vector $\mathbf{U}_i$ (Eq. 10).

$$D(\mathbf{X}) = \| (\mathbf{X} - \mathbf{P}_i) \wedge \mathbf{U}_i \| \quad (10)$$

3.1. Implementation

Given a scalar field, it is not possible to find an analytical solution to the implicit equation (Eq. 5). The resolution is done by the mean of the discretization of the volume containing the scalar field from which the surface is extracted. In the literature, the most common technique is to define the scene as a rectangular bounding box divided into voxels. Each of the vertex thus defined is associated with a field value. Within this discretization, the iso-surface extraction can be done with the marching cube algorithm [24]. The simulation of a particular test case requires to initialize the scalar field with values from the milling simulation presented in section 4.1. For each point of the grid, the new value is updated according to equation (Eq. 6). It should be noted that each vertex field value is independent from others. Moreover, the overall result defined by (Eq. 7) is not related to the order of the time step. These two affirmations allow implementing the simulation of the algorithm 1 into GPU architecture to benefit from massive parallelism.

The main drawback of this method is the volumetric discretization required. The number of vertices is inversely proportional to the cube of the spatial step. As a result, a small increase of the output resolution can lead to long computational time and great memory requirements. Simulation performances for test cases are given in section 6.

Algorithm 1: Pseudo-code for simulation

```
for each abrasive particle P_i do
    compute distance D between P_i and X
    evaluate K according to D
    subtract W_i from F_t(X)
end
extract surface from scalar field F_t
```

4. Complete process modeling

4.1. Machining simulation of surface

Machining has been simulated with the assumption of boolean operations between the tool and the workpiece in the literature [25]. The relevance of this hypothesis provides simulations that are very realistic, because in reality, the material removal due to cutting during machining generates precise surfaces. In order for the proposed approach to be compatible with the abrasion model developed, the implicit surface formalism has been chosen to simulate machined surface topography.

The definition of a given scalar field leads to a unique iso-surface at the prescribed iso-value. However, it is not possible to find a unique field corresponding to a given surface. The simplest way to circumvent this problem is to use the signed distance function. While the field may be straightforward to find for simple objects, composition operators are used to combine them together into more complex shapes. Since the distance field is positive inside the parts, the three basic boolean operators between fields F_{D_1} and F_{D_2} are defined in table 1.

Boolean operation	operator
Intersection	$F_D = min(F_{D_1}, F_{D_2})$
Difference	$F_D = min(F_{D_1}, -F_{D_2})$
Union	$F_D = max(F_{D_1}, F_{D_2})$

Table 1: Basic composition operators for implicit surfaces

The first step of the simulation of a machining operation consists in defining an initial distance field F_{D_0} which describes the initial raw surface of the part. In the presented study, the specimen before milling is considered as a perfect plane which results in the definition given in (Eq. 11). The scalar field T_i

associated with the tool is generally easy to determine since the shape is simple (cylinder, sphere, torus). The tool field can otherwise be obtained from composition of more simple fields. During the machining simulations the instances of the milling tool for each time step (T_i) are subtracted with the difference operator from the raw surface F_{D_0} in order to obtain the finish surface (Eq. 12). The operation is defined recursively from one step to another. The sequence of tool positions has no importance, thus the implementation of this algorithm can be efficiently done with parallel programming techniques. The resulting field of the machined surface is given by equation (Eq. 13).

$$F_{D_0} = -z \tag{11}$$

$$F_{D_n} = min(F_{D_{n-1}}, -T_n) \tag{12}$$

$$F_{D_n} = min(F_{D_0}, \{-T_i \mid i \in [1, n]\}) \tag{13}$$

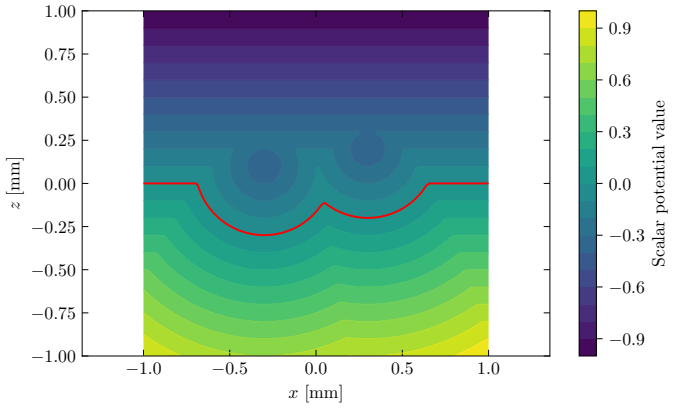

Figure 5: 2D machining example

An example of machining simulation is pictured in (Fig. 5). The simulation has been done in 2D for this simple example in order to show the resulting scalar field. The original surface is a straight line whose height is zero. The machined surface is obtained after two tool paths of a ball-end mill which generate a single scallop. The iso-level curves represent the distance field after the machining simulation and the specimen surface corresponds to the zero level curve plotted in red. This field that represents the milled topography is the input for the abrasion simulation presented later.

4.2. From distance field to initial surface potential

The simulation of (Eq. 7) requires to define an initial potential field F_{t_0}. Natural choice is the distance field F_{D_n} from the previous step of simulation. However, a modification of the field offers the opportunity to model the process behavior. In order to illustrate the key parameters playing a role in the field definition, a simple unidirectional case is considered.

In (Fig. 6), the surface of the specimen is represented as a point and the field values are plotted in abscissa. This figure corresponds to the magnifying of a small area around the specimen surface represented in (Fig. 7). At this scale, an elementary abrasive action dF is considered constant regardless of the position. As a consequence, the effect on the surface displacement dz depends on the gradient k of the field and is characterized by equation (Eq. 14).

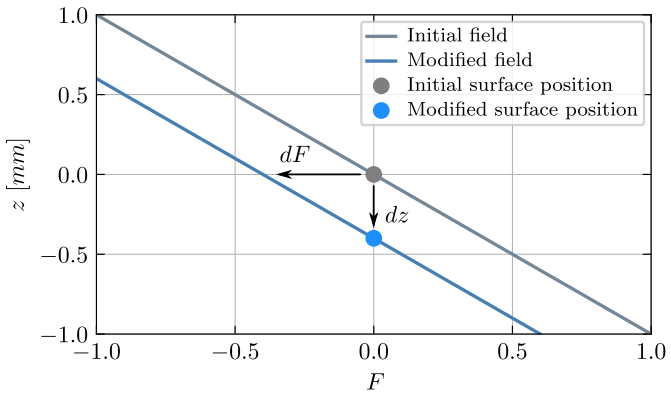

Figure 6: Initial field for specimen and effect of elementary abrasive action

$$\frac{\partial F_t}{\partial z}(z) = -\frac{1}{k} \tag{14}$$

The coefficient k is related to the specimen field by equation (Eq. 15). This equation is an analogy to the Preston model, thus the gradient of the field has an influence on the material removal rate in the implicit framework. Thus, the influence of pressure on the abrasion rate (Eq. 1), can be modeled by means of the setting parameter k.

$$k = \frac{1}{\|\nabla F_t\|} \tag{15}$$

During the simulation, the slope gradient increases as the specimen undergo the summation of the penalty field from the abrasive. This phenomenon encountered is highlighted with (Fig. 7). In this example, the abrasive field is subtracted from the initial scalar field which moves the surface position. Due to the fact that the abrasive field is not constant, the slope gradient of the specimen scalar field after abrasive action is increased, which in turn reduces the removal rate of the process (Eq. 16).

$$\|\nabla F_t\| > \|\nabla F_{t-1}\| \tag{16}$$

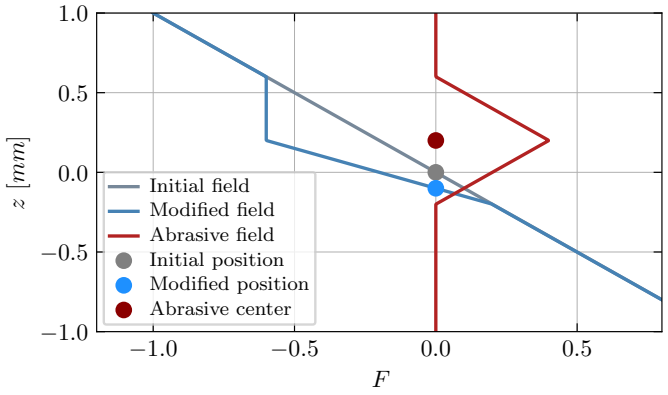

Figure 7: Unidirectional grain action

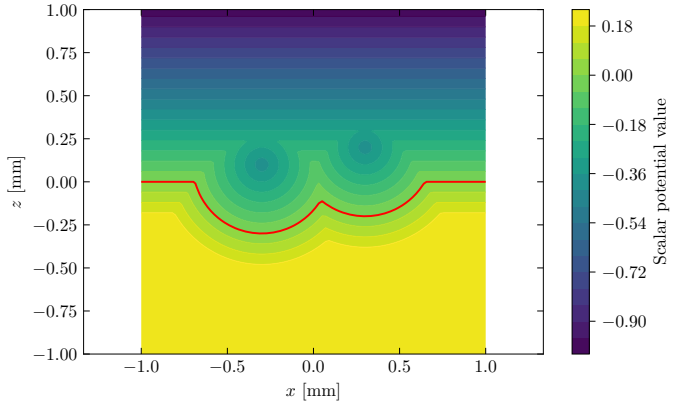

Figure 9: Initial potential example considering threshold distance

This behavior is a drawback when it comes to applying the implicit abrasion model to a real surface obtained from machining. In (Fig. 8), a raw machined surface with peaks and valleys is considered. This surface is embedded in a grid where field values are stored during the simulation run.

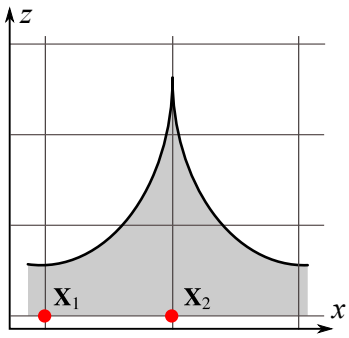

Figure 8: Effect of scallop height

Two points $\mathbf{X}_1$ and $\mathbf{X}_2$ are considered. The difference between these two points is their distances from the initial surface, $\mathbf{X}_1$ is under a valley and $\mathbf{X}_2$ is under a peak. The resulting field values for the two points are not the same but initial gradients are equal (Eq. 17).

$$\begin{cases} F_{t_0}(\mathbf{X}_1) < F_{t_0}(\mathbf{X}_2) \\ \nabla F_{t_0}(\mathbf{X}_1) = \nabla F_{t_0}(\mathbf{X}_2) = 1/k \end{cases} \tag{17}$$

Provided that after polishing, the surface has reached $\mathbf{X}_1$ and $\mathbf{X}_2$ due to a certain number of grain passages n_1 and n_2, the resulting field value is zero for both points (Eq. 18).

$$\begin{cases} F_t(\mathbf{X}_1) = F_{t_0}(\mathbf{X}_1) - \sum_{i=0}^{n_1} W_i\,(\mathbf{X}_1) = 0 \\ F_t(\mathbf{X}_2) = F_{t_0}(\mathbf{X}_2) - \sum_{i=0}^{n_2} W_i(\mathbf{X}_2) = 0 \end{cases} \tag{18}$$

The combination of (Eq. 17) and (Eq. 18) leads to a number of involved path $n_1 < n_2$ because the initial potential in $\mathbf{X}_2$ is higher than in $\mathbf{X}_1$. Thus the resulting gradient is not the same (Eq. 19).

$$\nabla F_t(\mathbf{X}_1) < \nabla F_t(\mathbf{X}_2) \tag{19}$$

This difference is not suitable because the gradient influences the removal rate of the simulated process, whereas the experimental removal rate is the same everywhere in the specimen once the machining scallops have been removed. This behavior results from the initial potential values inside the specimen which are not the same. For the model to be coherent toward the real process physics, the initial potential value must be constant over a certain distance from the specimen surface.

Given the previous analysis, two parameters have been proposed in order to define the transition from a distance field F_{D_n} resulting from the machining simulation to the initial scalar field F_{t_0} dedicated to abrasion simulation. F_{t_0} is defined as a function of F_{D_n} whose parameters are the inverse of the gradient k and a threshold β as stated in (Eq. 20). The parameter k accounts for the material removal rate and β is a distance threshold from which the field is constant. (Fig. 9) shows the result for the 2D milling example.

$$F_{t_0}(\mathbf{X}) = F_{t_0}(F_{D_n}) = \begin{cases} \frac{1}{k} F_{D_n} & F_{D_n} \leq \beta \\ \frac{1}{k}\beta & F_{D_n} > \beta \end{cases} \tag{20}$$

5. Simulation of grain path

The presented model in section 2 defines the core behavior of the interaction between an abrasive particle and the specimen. For a simulation to be performed, the grain path as well as the grain size are required inputs. In this section, the proposed method is presented and results are analyzed.

5.1. Grain path generation

For the simulation of the abrasion, the generation of abrasive particle path is mandatory. The relative motion between the abrasive tool and the workpiece is responsible for the material removal. Since the abrasive particle shapes and their motion are not regular, the exact geometry and path followed by each grain is not possible to determine but can be reasonably approximated locally.

For the simulation, the grain paths have been modeled by an evenly distributed set of lines over the interest area. Even if the test surface is not a perfect plane due to the scallop induced by the machining, its mean orientation remains horizontal and every generated path lines are also horizontal. The lines are defined by a point $\mathbf{P}_i$ and directed by a unit vector $\mathbf{U}_i$ whose definitions are given in equations (Eq. 21) and (Eq. 22).

$$\mathbf{P}_i = [\ r_i.cos(\theta_i),\ r_i.sin(\theta_i),\ z_i\ ] \tag{21}$$

$$\mathbf{U}_i = [\ -sin(\theta_i),\ cos(\theta_i),\ 0] \tag{22}$$

Let Δ be the width of the interest square area, r_i and θ_i are two random uniform variables whose ranges are respectively $[-\Delta/\sqrt{2}, \Delta/\sqrt{2}]$ and $[0, \pi]$. This parametrization allows to generate a set of lines (Eq. 25) as pictured in (Fig. 10).

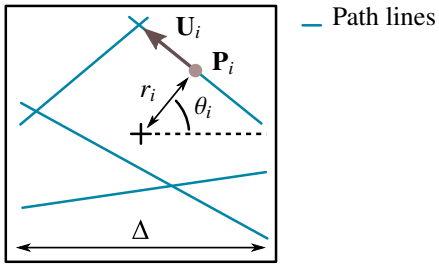

Figure 10: Line parametrization

The definition of grain paths requires to compute the number of paths against time given a certain abrasive paper characteristics defined by the *(ISO 6344)* standard.

$$n_g = V.J_g.\Delta.(t - t_0) \tag{23}$$

In (Eq. 23) the number of grain paths n_g is defined given process parameters. V is the relative velocity between the abrasive and the workpiece, J_g is the density of grains per surface unit. The number of grain paths is given by a time integration of the flux through the edge Δ. To simplify the simulation framework, it is possible to group the paths by sets of lines in the same plane, at a constant height from the average surface of the part (Eq. 24). This hypothesis is justified by the fact that the average height of the surface is significantly modified only after a certain number of grain passages. The third component of the unit vector $\mathbf{U}_i$ is set to zero for every line since the surface is assumed to be contained in a horizontal plane and the relative height of the lines z_k is constant for one set of lines L_k (Eq. 25). This leads to a total number of grains $n_g = m.n_k$.

$$M = \{L_k \mid k \in [1; m]\} \tag{24}$$

$$L_k = \{\ \mathbf{P}_i,\ \mathbf{U}_i \mid i \in [1; n_k],\ z_i = z_k\} \tag{25}$$

During the abrasion simulation, the value of the specimen field F_t is the results of all the previous grain passages before time t. The relative position of the grains from the surface leads to a certain interpenetration distance h. In order to avoid extracting the surface from the specimen scalar field at each time step, h is defined according to the overlapping volume Ω and the specimen surface S (Fig. 11) (Eq. 26).

$$\Omega = S.h \tag{26}$$

The overlapping volume is computed with F_t and W_z, which is a scalar field constructed from the mean value μ_g of the grain size distribution (Eq. 28). Thus, the overlapping volume Ω is the set of points where both fields are positive (Eq. 27). From a numerical point of view, the determination of this volume is straightforward because the implicit formalism allows evaluating each field sign on the spatial grid defined previously. The summation over all the points is done with a parallel reduction algorithm in order to compute the volume efficiently.

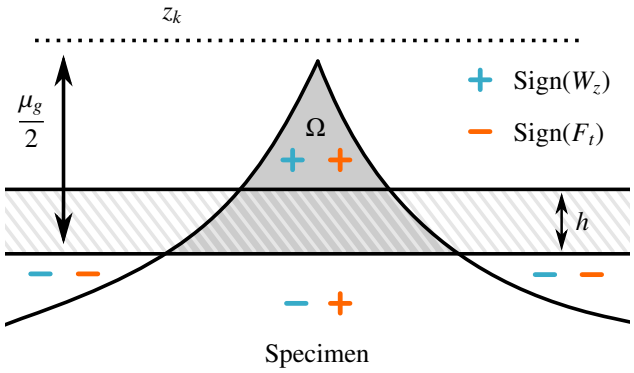

Figure 11: Overlapping volume for grain height computation

$$\Omega = \{\ \mathbf{X} \mid F_t(\mathbf{X}) > 0 \text{ and } W_z(\mathbf{X}) > 0\ \} \tag{27}$$

$$W_z(\mathbf{X}) = W_z(z) \begin{cases} 1 & |z - z_k| \leq \dfrac{\mu_g}{2} \\ -1 & |z - z_k| > \dfrac{\mu_g}{2} \end{cases} \tag{28}$$

The value of z_k is found by choosing a target value for h and by using an optimization algorithm.

5.2. Grain size distribution

The last step of the grain modeling is the definition of the size of the grains. Abrasive tools are mostly made of grains of calibrated size, coated together to a flexible substrate. The most commonly used material that composed abrasive grains is silicon carbide due to high Young's modulus and melting temperature. The abrasive paper characteristics are defined by the *ISO*

6344 standard. Grain diameter is a random variable which follows a probability distribution whose characteristic points are given in tables 2 and 3. For each point of the distribution d_{si} defined in these tables, the theoretical cumulative fraction Φ_{std} that the distribution follows is given in equation (Eq. 29).

Abrasive	d_{s0} [μm]	d_{s7} [μm]	d_{s42} [μm]	d_{s86} [μm]	d_{s96} [μm]
P120	212	150	125	106	90

Table 2: Grain size distribution for macro-grits coated abrasive

Abrasive	d_{s0} [μm]	d_{s3} [μm]	d_{s50} [μm]	d_{s95} [μm]
P240	110	81.7	58.5	44.5
P400	81	53.9	35	25.2
P600	72	43	25.8	18

Table 3: Grain size distribution for micro-grits coated abrasive

$$\Phi_{std}\ (d_{si}) = 1 - \frac{i}{100} \tag{29}$$

For the generation of a set of grains which is representative of the standard definition, the grain size is assumed to follow a normal distribution. As a consequence, the probability density chosen is the Gaussian function. The probability p_g to find a grain whose size is d_g is given by equation (Eq. 30). For each type of abrasive considered, the mean value μ_g of the distribution and the standard deviation σ_g must be found in order to numerically generate the corresponding random variable for the simulations. The missing values of μ_g and σ_g have been found by fitting the cumulative distribution function Φ_g (*Eq.* 31) to the characteristic points of grain size distribution defined in the standard by minimizing the error function e (Eq. 32). Note that the standard deviation of the distribution is equal to the value of d_{s50} for *P*240 and *P*600 abrasive without requiring to a constraint optimization. The results of the optimization is given in table 4 and the cumulative distribution function is plotted in (Fig. 12).

$$p_g\ (d_g) = \frac{1}{\sqrt{2\pi}\,\sigma_g}\, e^{-\frac{1}{2}\frac{(d_g-\mu_g)^2}{\sigma_g^2}} \tag{30}$$

$$\Phi_g\ (d_g) = \frac{1}{2}\left[1 + erf\left(\frac{d_g-\mu_g}{\sqrt{2}\,\sigma_g}\right)\right] \tag{31}$$

$$e\ (\mu_g, \sigma_g) = \sum_i \left(\Phi_{std}(d_{si}) - \Phi_g(d_{si})\right)^2 \tag{32}$$

Abrasive type	μ_g [μm]	σ_g [μm]
P120	122.3	16.4
P240	58.5	8.8
P400	35.0	6.0
P600	25.8	4.8

Table 4: Normal distribution parameters

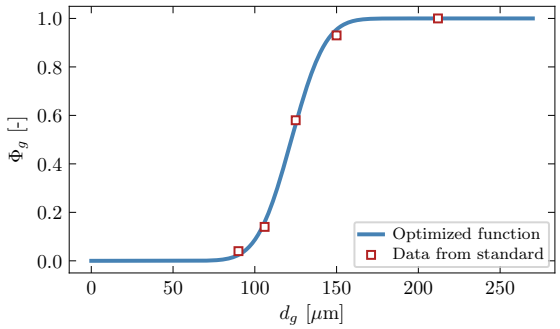

Figure 12: Optimization of distribution parameters for P120

Based on the height z_k and provided that not all particles have same diameter d_g, three position schemes have been considered (Fig. 13). Either the center of each particle is aligned or shifted toward bottom or top. For the test cases considered in this article, the second configuration has been chosen otherwise the grooves generated by the largest particles are too prevalent.

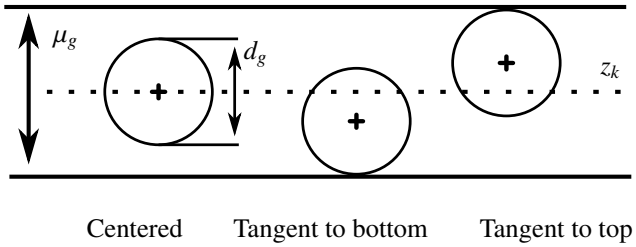

Figure 13: Position of particles

6. Experimental validations

6.1. Case 1: automatic polishing

The experimental validation of the proposed method is carried out on a test case including a finishing milling phase followed by an automatic polishing phase performed on a Mikron UCP710 machining center as described in [26] (Fig. 14 -right). The application targeted is the production of plastic injection molds and the material is a X38CrMoV5 steel with the hardness of 53 HRC. Milling is carried out with a hemispherical tool of 10mm diameter which is a solid carbide end mill for profiling from Sandvik Coromant.

In this example, the milling strategy includes parallel paths and a relatively small feed per tooth which leads to a surface

with parallel scallops. The distance between passes is 1 *mm*. Topography resulting from the implicit simulation of the milling operation is presented in figure 15. The implicit framework applied for the milling simulation behaves as expected and produces surface topography which corresponds to the experimental measurement.

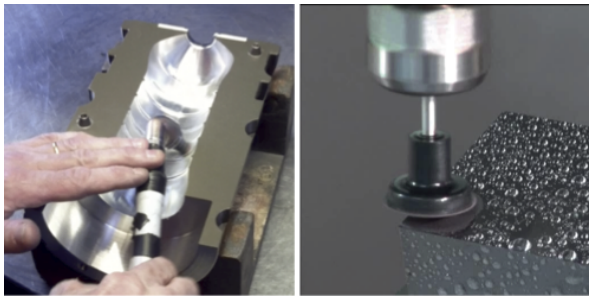

Figure 14: Abrasion processes

The tools used for polishing are abrasive disks whose diameter is 18 mm. The abrasive grains are composed of silicon carbide. The disks are pasted on a flexible elastomer support. The deformation of the elastomer allows the abrasive tool to conform to the surface and the force is adjusted by changing the relative distance between the tool and the workpiece. The spindle speed for abrasive tools is set to 2000 rpm. The polishing operations are carried out with a tilt angle of the tool in the feed direction equal to 10° and an imposed dispacement of 1mm, leading to a polishing force of 10N [26]. Thus, only a portion of the disk in its peripheral area is in contact with the part [27] which leads to a cutting speed of 110 m/min. The polishing operation is a succession of three different grades (grade 120, 240 and 600) and the abrasion process has been separated into four steps : grade 120 along X-axis ; grade 120 along Y-axis ; grade 240 ; grade 600. The measurement of the surface topography is done in situ after each stage of the abrasive process without removing the workpiece [28].

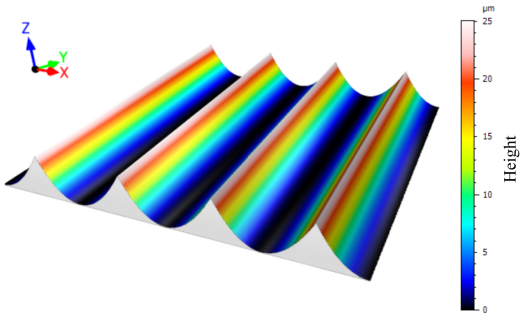

Figure 15: Implicit machining simulation

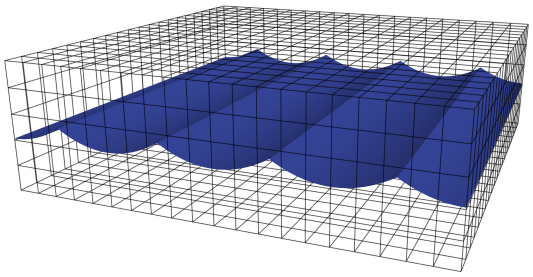

Figure 16: Extraction of surface

The sensor used to measure the surface topography is an optical device from STIL [29]. Its technology is based on a confocal chromatic sensor. The incident white light is dispersed along the Z-axis. The focused wavelength of the reflected beam is determined in order to obtain the position of the surface in the measuring field with high resolution. The measurement is made every 0.01 mm on a surface of 1 mm by 4 mm.

Case	Test case 1	Test case 2
Length x [mm]	4	1.2
Width y [mm]	4	0.7
Height z [mm]	0.12	0.12
Step x [mm]	0.02	0.004
Step y [mm]	0.02	0.004
Step z [mm]	0.003	0.0003
Number of points	16, 200, 801	21, 122, 675

Table 5: Simulation grid characteristics

The simulation is computed in a local area of the part with the grid characteristics presented in table 5. This space discretization is required to perform the surface extraction (Fig. 16) with the marching cube algorithm [24]. The overall dimensions of the working area are given as well as the size of the discretization steps in each direction. The simulations have been carried out with the following hardware configurations:

- Xeon CPU: Intel Xeon Processor E5-1620V3, 3.5 Ghz, 31 Gflops DP, 4 cores, 8 threads
- GeForce GTX Titan Z (one GK110 GPU): 705 MHz, 2×6GB (GDDR5), 2880 CUDA cores.

The complete modeled abrasion process is presented in table 7. In these simulations, β must be smaller than the height of the marks left by machining but sufficiently high to be able to correctly simulate the passage of the grains. A value of 3 μm for β and 1 for k has been used in all the test cases. This configuration leads to the simulation times presented in table 6.

Case	Simulation time
Test case 1	41 *sec*
Test case 2 - P240	48 *sec*
Test case 2 - P400	45 *sec*

Table 6: Simulation time

The parameters for the different steps are determined regarding the paper size and measured topography. The first two steps with paper P120 (Fig. 17) have the same parameters and match the experimental profile. The first step is used in order to identify the process parameters (n_g and h) by an optimization between simulation and experimental results. The second step is simulated with the same set of parameters because these two steps are realized with the same paper and the same process characteristics. This shows the ability of the proposed model to adapt to any initial topography for a tool workpiece pair. Besides, the effect of initial topography on the abrasion rate is coherent with experimental measurement. When the bearing area of the specimen increases, the abrasion rate obtained in the simulation decreases as expected from the measurements (Fig. 18). In this figure, the thin-line data correspond to experimental measurements and the simulations are displayed with thick lines. The last two steps with paper P240 and P600 completely remove milling scallops in the experiment as well as in the simulation. Once the bottom of the scallops has been reached by the abrasive paper, the abrasion rate is constant over the surface of the specimen regardless of the initial surface topography. As presented in section 4.2, this has been made possible in the model with the limitation of the potential field by threshold β. Table 8 presents the associated surface roughness parameters S_a. It can be observed that the simulated results are coherent with the measurement. Roughness of milled surface is higher in the simulation because the simulated surface has sharp edges contrary to the experimental one. The last step is smoother than the experimental topography because the simulation tends to generate smooth surfaces while the experimental surfaces show peeling phenonema that become significant once the machining marks are removed.

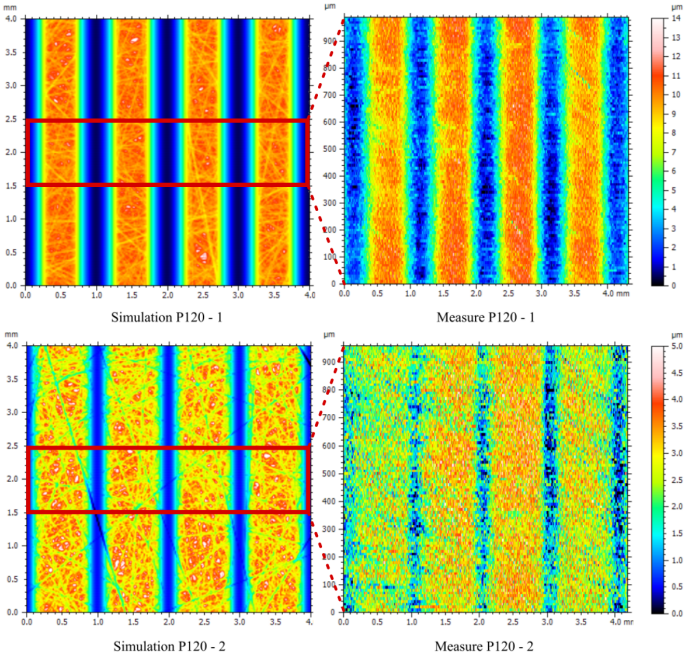

Figure 17: Simulated and measured topography

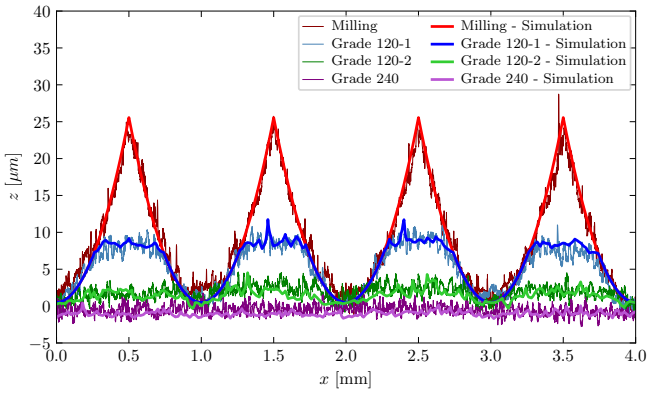

Figure 18: Simulated (bold lines) and measured profiles (thin line)

Abrasion step	Abrasive type	n_g	h [$\%d_g$]
Polishing grade 120-x	P120	900	1.8 %
Polishing grade 120-y	P120	900	1.8 %
Polishing grade 240	P240	1800	1.8 %
Polishing grade 600	P600	2400	1.8 %

Table 7: Simulation parameters - Automatic polishing

Abrasion step	Experimental	Simulated
Milling	5.77	6.34
Grade 120-1	2.80	2.69
Grade 120-2	0.76	0.67
Grade 240	0.55	0.27

Table 8: Surface roughness analysis S_a - [μm]

6.2. *Case 2: manual polishing*

The second example concerns a manufacturing process integrating a finishing milling phase followed by manual polishing operations conducted by a skilled operator (Fig. 14 - left). The targeted application is the production of molds for blowing plastic bottles and the material is an aluminium alloy AlZn5Mg3Cu [30]. During the milling, the feed per tooth is not negligible with respect to the feed direction. In this case, the generated pattern can be approximated by a succession of spherical cups for each tooth revolution. Thus the longitudinal interval is the feed per tooth. This pattern depends only on the feed per tooth, the transverse step and the radius of the tool. Topography resulting from the implicit milling simulations is presented in (Fig. 19). One can notice that the resulting topography is very different from case 1, especially in terms of bearing area. Regarding the abrasion process, it consists of two stages with 240 and 400 grade abrasives from the milled state. The simulation is computed with the grid characteristics presented in table 5.

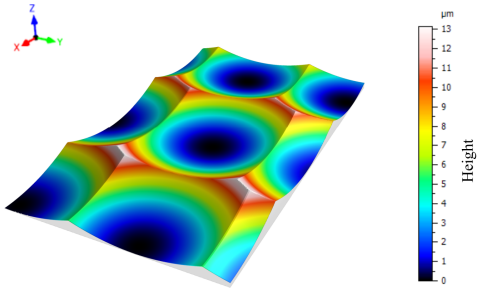

Figure 19: Implicit machining simulation - test case 2

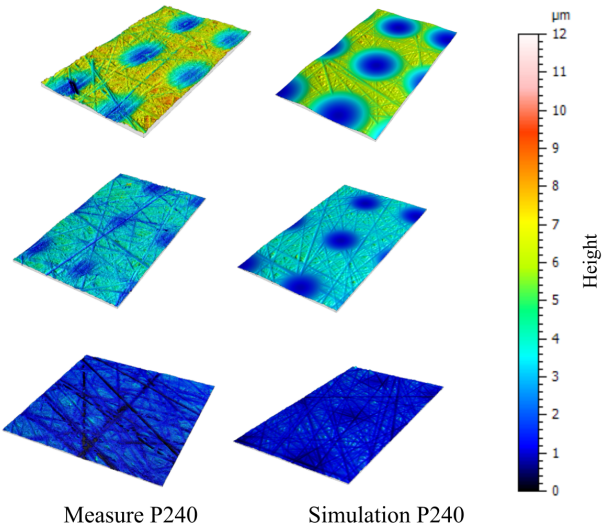

Figure 20: Simulated and measured topography for manual polishing process

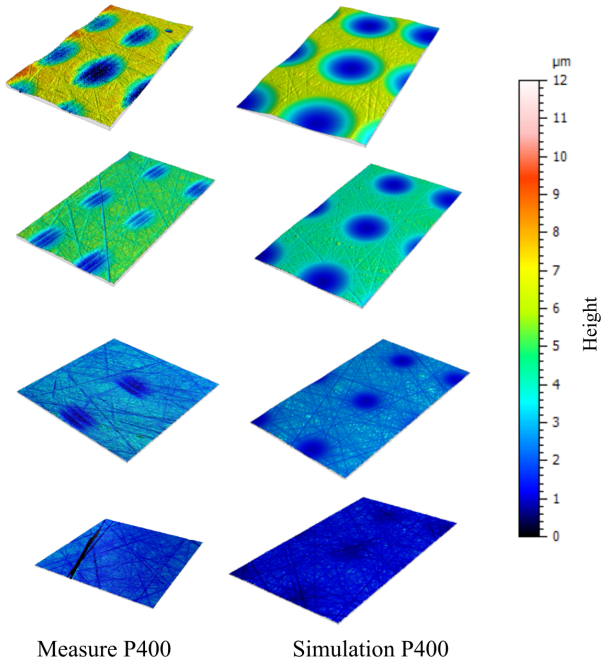

Figure 21: Comparison for P400 grade

Abrasion step	Experimental	Simulated
Milling	2.77	2.32
Grade 240-1	1.35	1.42
Grade 240-2	0.60	0.57
Grade 240-3	0.45	0.26

Table 9: Surface roughness analysis for abrasive grade 240 - [μm]

Abrasion step	Experimental	Simulated
Milling	2.77	2.32
Grade 400-1	1.77	1.57
Grade 400-2	0.71	0.81
Grade 400-3	0.37	0.30
Grade 400-4	0.37	0.17

Table 10: Surface roughness analysis for abrasive grade 400 [μm]

For both abrasive grades, a single set of parameters for each step allows obtaining a representative abrasion simulation. The same method for finding the simulation parameters is used than for test case 1. Fig. 20 presents the respective topographies for the P240 and P400 papers. These two additional cases show that the abrasion with different paper sizes can be taken into account. The bottoms of the scallops are not affected in the simulations because the path of the grains is considered to be a straight line independently from the real surface topography. As a consequence the scallops are still slightly visible in the simulations whereas they have been removed experimentally.

Roughness parameters are listed in tables 9 and 10 for both

abrasive papers. The same correlation between simulation and experimental data is observed. The roughness in the two last steps is still significanly lower in the simulations. The model tends to generate smooth surfaces whereas the random character of the abrasion may result in additional grooves that are not taken into account. This can be observed visually in the figures 20 and 21. Event if the parameters of the manual polishing process may be hard to evaluate, the simulation framework provides results that are relevant provided the repeatability of the skilled operator.

7. Conclusion and future works

A novel numerical model to simulate finishing processes has been proposed. This model is based on an implicit representation of surfaces and a proper definition of the potential field associated to each grain path for the simulation of the material removal encountered during abrasion. The implementation of an implicit milling simulation has been integrated into the implicit abrasion framework in order to take into account the scallop induced during milling. The simulation of a complete manufacturing process from milling to finishing has been performed and compared to the experiments. The simulated surfaces are coherent with experimental measurements. The grain size distributions of the abrasive papers have been taken into account in the simulation. The grains are considered as spheres, but it is possible to implement other shapes in the implicit framework. The succession of simulation steps is coherent with the measured ones and the abrasion rate is reduced when the bearing area of the surface increases. The computation time in all the test cases is less than one minute with conventional desktop hardware. The order of magnitude of computation time is already compatible with industrial requirements without major optimization of the implementation.

In the presented model, the generation of the abrasive potential field, which takes into account the grain paths and the local interaction characteristics, is done with geometric considerations. The relation between the effort and the grain path is the next development considered for the proposed model. In order to take into account the pressure as an input for the model, a relation between the pressure and the overlapping volume should be studied. This extension will be integrated in the grain path generation in order to determine the relative height of the grains.

In this study, the specimen areas taken into account are relatively small thus it is justified to assume that the global curvature of the surface is null. The simulation of abrasion in case of complex surfaces seems achievable using conformal mapping between the real surface and a plane and would not require major modifications of the simulation framework. The preliminary results of the model could be used to find the optimum parameters of an overall optimization of the manufacturing process including milling and abrasion finishing.

References

[1] F. Hashimoto, H. Yamaguchi, P. Krajnik, K. Wegener, R. Chaudhari, H.-W. Hoffmeister, F. Kuster, Abrasive fine-finishing technology, CIRP Annals 65 (2016) 597–620.

[2] K. Wegener, F. Bleicher, P. Krajnik, H.-W. Hoffmeister, C. Brecher, Recent developments in grinding machines, CIRP Annals 66 (2017) 779–802.

[3] F. Klocke, O. Dambon, B. Behrens, Analysis of defect mechanisms in polishing of tool steels, Production Engineering 5 (2011) 475–483.

[4] C. Cheng, J. Li, Y. Liu, M. Nie, W. Wang, Deep convolutional neural network-based in-process tool condition monitoring in abrasive belt grinding, Computers in Industry 106 (2019) 1–13.

[5] S. Lavernhe, Y. Quinsat, C. Lartigue, C. Brown, Realistic simulation of surface defects in five-axis milling using the measured geometry of the tool, The International Journal of Advanced Manufacturing Technology 74 (2014) 393–401.

[6] S. Ratchev, S. Nikov, I. Moualek, Material removal simulation of peripheral milling of thin wall low-rigidity structures using FEA, Advances in Engineering Software 35 (2004) 481–491.

[7] M. Jachym, S. Lavernhe, C. Euzenat, C. Tournier, Effective NC machining simulation with OptiX ray tracing engine, The Visual Computer 35 (2018) 281–288.

[8] J. Zhang, S. Ong, A. Nee, Design and development of an in situ machining simulation system using augmented reality technology, Procedia CIRP 3 (2012) 185–190.

[9] F. Abecassis, S. Lavernhe, C. Tournier, P.-A. Boucard, Performance evaluation of CUDA programming for 5-axis machining multi-scale simulation, Computers in Industry 71 (2015) 1–9.

[10] W.-L. Zhu, Y. Yang, H. N. Li, D. Axinte, A. Beaucamp, Theoretical and experimental investigation of material removal mechanism in compliant shape adaptive grinding process, International Journal of Machine Tools and Manufacture 142 (2019) 76–97.

[11] S. Leroch, M. Varga, S. Eder, A. Vernes, M. R. Ripoll, G. Ganzenmüller, Smooth particle hydrodynamics simulation of damage induced by a spherical indenter scratching a viscoplastic material, International Journal of Solids and Structures 81 (2016) 188–202.

[12] G. Kermouche, J. Rech, H. Hamdi, J. Bergheau, On the residual stress field induced by a scratching round abrasive grain, Wear 269 (2010) 86–92.

[13] J. Jiang, P. Ge, W. Bi, L. Zhang, D. Wang, Y. Zhang, 2d/3d ground surface topography modeling considering dressing and wear effects in grinding process, International Journal of Machine Tools and Manufacture 74 (2013) 29–40.

[14] W. Ding, C. Dai, T. Yu, J. Xu, Y. Fu, Grinding performance of textured monolayer CBN wheels: Undeformed chip thickness nonuniformity modeling and ground surface topography prediction, International Journal of Machine Tools and Manufacture 122 (2017) 66–80.

[15] J. Aurich, B. Kirsch, Kinematic simulation of high-performance grinding for analysis of chip parameters of single grains, CIRP Journal of Manufacturing Science and Technology 5 (2012) 164–174.

[16] C. Euzenat, S. Lavernhe, C. Tournier, Implicit modeling of abrasion process based on potential field, Computer-Aided Design 110 (2019) 69–77.

[17] E. Brinksmeier, J. Aurich, E. Govekar, C. Heinzel, H.-W. Hoffmeister, F. Klocke, J. Peters, R. Rentsch, D. Stephenson, E. Uhlmann, K. Weinert, M. Wittmann, Advances in modeling and simulation of grinding processes, CIRP Annals 55 (2006) 667–696.

[18] K. Z. Gahr, Preface (1987) v–vi.

[19] F. W. Preston, The theory and design of plate glass polishing machine, J. soc. Glass technol 11 (1927) 214–256.

[20] K.-H. Gahr, Wear by hard particles, Tribology International 31 (1998) 587–596.

[21] L. Barthe, N. A. Dodgson, M. A. Sabin, B. Wyvill, V. Gaildrat, Two-dimensional potential fields for advanced implicit modeling operators, Computer Graphics Forum 22 (2003) 23–33.

[22] J. Bloomenthal, B. Wyvill, Interactive techniques for implicit modeling, SIGGRAPH Comput. Graph. 24 (1990) 109–116.

[23] J. Bloomenthal, B. Wyvill (Eds.), Introduction to Implicit Surfaces, Morgan Kaufmann Publishers Inc., San Francisco, CA, USA, 1997.

[24] W. E. Lorensen, H. E. Cline, Marching cubes: A high resolution 3d surface construction algorithm (1987).

[25] W.-H. Zhang, G. Tan, M. Wan, T. Gao, D. H. Bassir, A new algorithm for the numerical simulation of machined surface topography in multiaxis ball-end milling, Journal of Manufacturing Science and Engineering 130 (2008).

[26] X. Pessoles, C. Tournier, Automatic polishing process of plastic injection molds on a 5-axis milling center, Journal of Materials Processing Technology 209 (2009) 3665–3673.

[27] A. Guiot, S. Pattofatto, C. Tournier, L. Mathieu, Modeling of a polishing tool to simulate material removal, Advanced Materials Research 223 (2011) 754–763.

[28] Y. Quinsat, C. Tournier, In situ non-contact measurements of surface roughness, Precision Engineering 36 (2012) 97–103.

[29] Fundamental Principles of Engineering Nanometrology, Elsevier, 2010. URL: https://doi.org/10.1016/c2009-0-20339-4. doi:10.1016/c2009-0-20339-4.

[30] L. Grandguillaume, S. Lavernhe, Y. Quinsat, C. Tournier, Mold manufacturing optimization: A global approach of milling and polishing processes, Procedia CIRP 31 (2015) 13–18.

Nomenclature

Implicit model

$\alpha_k, \mu_k, \sigma_k$	Kernel parameters	[-]	F_{t_0}	Scalar field of initial surface	[-]
$\mathbf{X} = (x,\ y,\ z)$	Coordinates of a point	[m]	K	Abrasive grain kernel	[-]
Γ	Set of points of the implicit surface		l	Input variable of kernel K	[m]
D	Distance function	[m]	W_i	Scalar field of abrasive particle i	[-]
F_t	Scalar field	[-]			

Complete process modeling

β	Field threshold distance	[m]	F_{D_0}	Signed distance field of raw surface	[m]
dF	Elementary abrasive action	[-]	F_{D_n}	Signed distance field after machining	[m]
dz	Elementary surface displacement	[m]	k	Inverse of field gradient	[-]
F_D	Signed distance field	[m]	T_i	Milling tool distance field	[-]

Simulation of grain path

$\mathbf{P}_i$	Passage point of path i	[m]	m	Number of line sets in M	[-]
$\mathbf{U}_i$	Unit vector of path i	[-]	n_g	Number of grain paths between t_0 and t_1	[-]
Δ	Width of interest area	[m]	n_k	Number of paths in L_k	[-]
Ω	Overlapping volume	[m^3]	r_i	Unit vector of path i	[-]
θ_i	Orientation of path i	[-]	S	Specimen area	[m^2]
h	Mean interpenetration distance	[m]	V	Relative velocity	[$m.s^{-1}$]
J_g	Grain density	[m^{-2}]	W_z	Scalar field based on grain size distribution	[-]
L_k	Set of lines for height z_k	[-]	z_k	height of paths in L_k	[m]
M	Complete set of lines	[-]			

Grain size modeling

μ_g	Mean value of grain size distribution	[μm]	d_g	Grain diameter	[μm]
Φ_g	Cumulative distribution	[-]	d_{si}	Grain size distribution value from standard	[μm]
Φ_{std}	Grain size cumulative fraction from standard	[-]	e	Error between standard and identified data	[-]
σ_g	Standard deviation of grain size distribution	[μm]	p_g	Probability density of grain size distribution	[-]